

# Chelation-Assisted Selective Etching Construction of Hierarchical Polyoxometalate-Based Metal–Organic Framework

Zhong Zhang, Yunwen Tao, Hongrui Tian, Qian Yue, Shumei Liu, Yiwei Liu, Xiaohui Li, Ying Lu, Zhixia Sun, Elfi Kraka, and Shuxia Liu\*

Cite This: *Chem. Mater.* 2020, 32, 5550–5557

Read Online

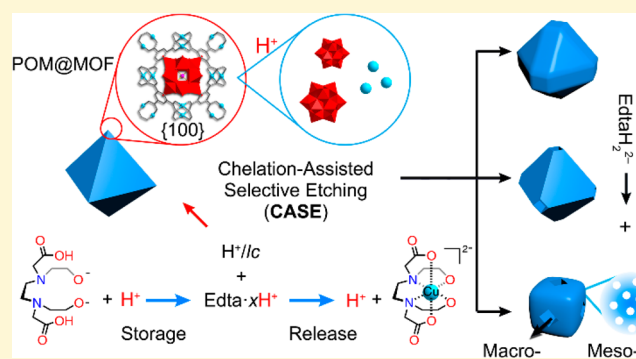
ACCESS |

Metrics & More

Article Recommendations

Supporting Information

**ABSTRACT:** A chelation-assisted selective etching (CASE) strategy is developed to construct a hierarchical polyoxometalate-based metal–organic framework (POM@MOF). The selected chelator, ethylenediaminetetraacetic dianion ( $\text{EdtaH}_2^{2-}$ ), can bind protons of the acid etchant to provide a low initial proton concentration. The dwindling protons are more controllable when localized at specific positions (e.g., polar crystal facets) of POM@MOF to initiate selective etching. Subsequently, with the liberated metal ions being chelated, the bound protons are gradually released in situ. The secondary release of protons results in a local high proton concentration (i.e., enrichment effect), thereby further enhancing the etch selectivity. When the amount of  $\text{EdtaH}_2^{2-}$  is controlled, POM@MOFs with different morphologies and pore structures are fabricated by selective etching. The on-demand



storage and release of protons overcomes the traditional uncontrollability caused by direct proton addition. The CASE strategy provides a feasible way to design diverse hierarchical MOFs because of the universal chelation between  $\text{EdtaH}_2^{2-}$  and metal ions.

## INTRODUCTION

Metal–organic frameworks (MOFs) are a class of crystalline porous materials built from metal ions/clusters with organic bridging linkers.<sup>1</sup> Because of their extraordinary porosity and abundant active sites, MOFs are widely used as catalysts<sup>2,3</sup> or catalyst supports.<sup>4,5</sup> A variety of functional guests or active species such as metal nanoparticles, polyoxometalates (POMs), enzymes, polymers, etc. can be supported in MOFs.<sup>4,5</sup> Compared with other guests, POMs, as a class of well-defined molecular clusters holding nano dimensions and specific geometry, can be integrated with MOFs by crystallization to form crystalline polyoxometalate-based metal–organic frameworks (POM@MOFs).<sup>6,7</sup> By virtue of the integrated merits of MOFs and POMs, POM@MOFs exhibit an excellent performance and heterogeneity in catalytic applications.<sup>8</sup> More importantly, the definite crystalline structure provides a convenient platform for studying mechanisms involving synthesis,<sup>9,10</sup> modulation,<sup>11,12</sup> modification,<sup>13,14</sup> catalysis,<sup>15,16</sup> etc.

Despite the molecular level dispersion of active POM clusters by MOF supports, the microporous skeleton (<2 nm) of MOFs inevitably hinders the accessibility of the catalytic POM sites inside or slows the diffusion kinetics of bulky reactants or products.<sup>6</sup> The construction of a hierarchical structure is widely considered as an alternative way to overcome the microporous limitation.<sup>17–20</sup> The macrovoid

or mesoporous structure can effectively promote mass transfer,<sup>17–20</sup> while intrinsic micropores can encapsulate POM<sup>6</sup> and retain adsorption performance.<sup>21</sup>

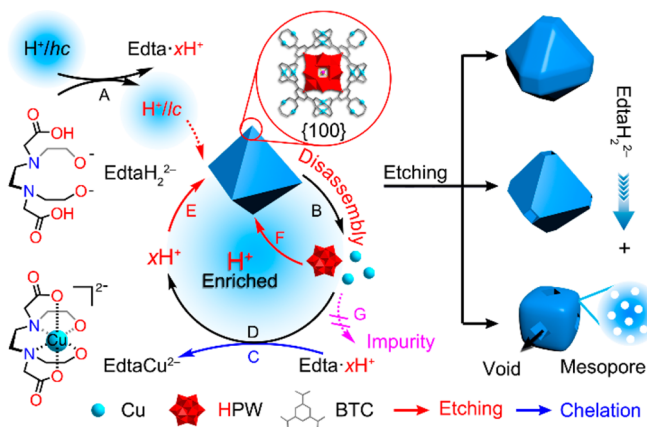
Acid etching is an effective way for constructing hierarchical MOFs.<sup>22–24</sup> As the reverse reaction of MOF assembly, the protonation of ligands can naturally break coordination bonds, i.e., the etching process. Due to the definite periodic structure and anisotropy of crystals, etching usually occurs selectively at specific locations<sup>22,25</sup> or crystal facets<sup>24</sup> to form macro-mesopores or the desired morphology. However, this selectivity is difficult precisely control because homogeneously dissolved protons can attach to every possible position of the MOFs. Herein, we develop a chelation-assisted selective etching (CASE) strategy for the construction of hierarchical POM@MOF (Scheme 1). This approach involves ethylenediaminetetraacetic dianion ( $\text{EdtaH}_2^{2-}$ ) as an aided-etching chelator, which can serve four purposes. First,  $\text{EdtaH}_2^{2-}$  can bind with protons of the acid etchant to provide a low initial proton concentration for initiating selective etching, which is

Received: February 4, 2020

Revised: June 7, 2020

Published: June 8, 2020



Scheme 1. Illustration of the CASE Process<sup>a</sup>

<sup>a</sup>hc/lc: high/low concentration.

ascribed to the decreasing protons being more controllably confined to some special locations. Second, the chelation between the chelators and the liberated metal ions significantly promotes the etching, originating from the broken equilibrium of MOF disassembly. Third, protonated chelators can release protons in situ after chelating metal ions, and the secondary release of protons results in a local high proton concentration (i.e., enrichment effect), further improving the precision of etching. Finally, the capture of metal ions inhibits further reactions, affording the pure-phase etched POM@MOF without concomitant impurities. To demonstrate the chelation-assisted selective etching, NENU-3a ( $[\text{Cu}_{12}(\text{BTC})_8][\text{H}_3\text{PW}_{12}\text{O}_{40}]$ ) (Figure S1),<sup>6</sup> assembled from Keggin  $\text{H}_3\text{PW}_{12}\text{O}_{40}$  (HPW),  $\text{Cu}^{2+}$ , and 1,3,5-benzenetricarboxylic acid ( $\text{H}_3\text{BTC}$ ) is selected as a study object. When the amount of  $\text{EdtaH}_2^{2-}$  added is controlled, the  $\{100\}$  crystal planes of NENU-3a can be selectively etched to a different extent, affording etched NENU-3a with a different morphology and porous structure (Scheme 1). It is worth mentioning that a related MOF etching technique based on pH and chelating agent was reported by Avci et al.,<sup>24</sup> however, their approach achieved anisotropic etching due to the differences in the number of coordination bonds for each crystal plane instead of the dynamic adjustment in the proton concentration via chelator as highlighted in this work. Because of the universal chelation between chelators and metal ions, this CASE strategy is expected to be applied to controllable synthesis of other hierarchical MOFs.

## RESULTS AND DISCUSSION

### Morphological Evolution in the Selective Etching.

The monodispersed NENU-3a octahedrons (around 2  $\mu\text{m}$ ) (Figures 1A and S2) were crystallized in the mixed solvents of chloroform and methanol (MeOH). According to our previous research, low-polar chloroform can effectively promote the crystallization as well as coordinate the nucleation versus growth of NENU-3a, resulting in uniform particles with regular morphology.<sup>17</sup> The phase purity of NENU-3a was confirmed by powder X-ray diffraction (XRD) and Fourier transform infrared (FT-IR) spectroscopy (Figure S3). When one takes into account the acid stability of NENU-3a (Figure S4A),<sup>14</sup> medium strong phosphoric acid ( $\text{H}_3\text{PO}_4$ ) was used as an etchant. In order to promote the  $\text{H}_3\text{PO}_4$  dissociation and provide a good solubility environment for released compo-

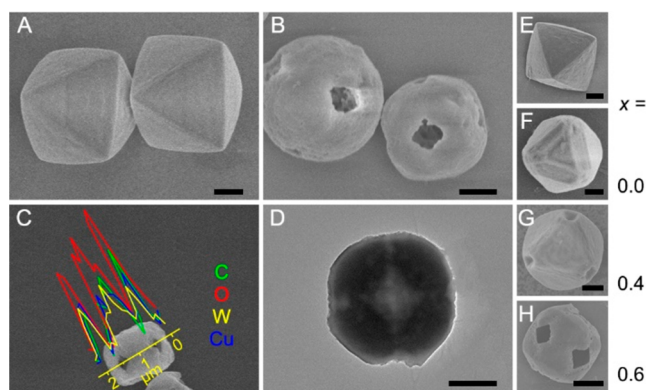


**Figure 1.** SEM images of monodispersed NENU-3a (A) and NENU-3a/0.6 (B). (C) EDX elemental line scanning and (D) TEM image of NENU-3a/0.6. (E–H) The morphology evolution from NENU-3a to NENU-3a/ $x$ . Scale bars: 500 nm.

nents against the secondary formation of NENU-3a, a mixed solvent of  $\text{H}_2\text{O}/\text{MeOH}$  (V/V, 1/1) was selected as the etching medium. As expected, NENU-3a was not etched significantly at low  $\text{H}_3\text{PO}_4$  concentration, except that the corners were slightly rounded (Figure S4B). However, NENU-3a completely collapsed, and an unknown phase formed when the concentration of  $\text{H}_3\text{PO}_4$  is too high (Figures S4D and S5). When 60 mM  $\text{H}_3\text{PO}_4$  was used, NENU-3a was etched significantly at the edges and corners (Figure S4C) (i.e., the  $\{110\}$  and  $\{100\}$  crystal planes, Figure S6), which may be because of the stronger affinity between exposed HPW on the  $\{100\}$  facet/ $\text{Cu}^{\text{II}}$  on the  $\{110\}$  facet and  $\text{H}^+$  (Figure S1A–C). It is worth noting that NENU-3a is stable in  $\text{NaH}_2\text{PO}_4$  solution and rapidly collapses in the hydrochloric acid solution (Figure S4E,F), which indicates that the H cation rather than the phosphate anion is the key in etching. The optimized  $\text{H}_3\text{PO}_4$  concentration, 60 mM, is used for the subsequent etching experiments. However, the concomitant impurity also appeared, which may be attributed to the second deposition of the liberated  $\text{Cu}^{2+}$  (Figure S5).

It is feasible to convert the released  $\text{Cu}^{2+}$  into a stable soluble species, in order to eliminate the impurity phase. Ethylenediaminetetraacetic acid ( $\text{EdtaH}_4$ ), as an important chelator, is widely used for complex titration in analytical chemistry because it can form hydrosoluble strong 1:1 complexes with most metal ions (Figure S7).<sup>26</sup> After the introduction of Edta disodium salt ( $\text{EdtaH}_2\text{Na}_2$ ), as expected, the unknown impurity disappeared (Figure S8A). FT-IR spectroscopy did not detect any residues of Edta species (Figure S8B), coinciding with the inability of large-size  $\text{EdtaH}_2^{2-}$  to enter the micropores of NENU-3a (Figure S7D). Surprisingly, the morphology of the etched NENU-3a changed significantly after the addition of  $\text{EdtaH}_2\text{Na}_2$ . For simplification, the etched NENU-3a is denoted as NENU-3a/ $x$  ( $x$  is the mass ratio of  $\text{EdtaH}_2\text{Na}_2$  added and NENU-3a). With the addition of  $\text{EdtaH}_2\text{Na}_2$  ( $x = 0.4$ ), selective etching on the  $\{100\}$  facets obviously occurred instead of appearing on both the  $\{100\}$  and  $\{110\}$  planes at the same time (Figure S4C), which can be concluded from the shallow holes at the vertexes of NENU-3a/0.4 (Figures 1G and S9). With the increase of  $\text{EdtaH}_2\text{Na}_2$ , the etching of the  $\{100\}$  crystal facet further deepened, affording the rounded cube with voids (NENU-3a/0.6, Figures 1B and S10). The undulating distribution of elements in energy dispersive X-ray (EDX) elemental line

scanning also indicates the definite void structure in NENU-3a/0.6 (Figures 1C and S11). As shown in transmission electron microscopy (TEM) images (Figures 1D and S10B1), the interconnected areas with low contrast inside the particles further confirms that the through void structure of NENU-3a/0.6 is evidently derived from the selective etching of six {100} crystal facets. The morphology evolution of NENU-3a/*x* is presented in Figure 1E–H and illustrated in Scheme 1. It is worth noting that, in the absence of H<sub>3</sub>PO<sub>4</sub>, the etching by EdtaH<sub>2</sub>Na<sub>2</sub> only occurred on the crystal surface (Figure S12), indicating that selective etching originates from the synergistic action between H<sup>+</sup> and EdtaH<sub>2</sub><sup>2-</sup>.

**Mechanism of Selective Etching.** According to our previous research, the cubic NENU-3a exhibits better catalytic and adsorption performance than that of the octahedral counterpart, owing to the exposure of HPW on the {100} facets.<sup>11</sup> In addition, compared with Cu<sub>3</sub>(BTC)<sub>2</sub>, the higher water and methanol adsorption capacity of NENU-3a indicates the strong interaction and affinity between HPW and polar molecules (Figure 2).<sup>17</sup> Density functional theoretical (DFT)

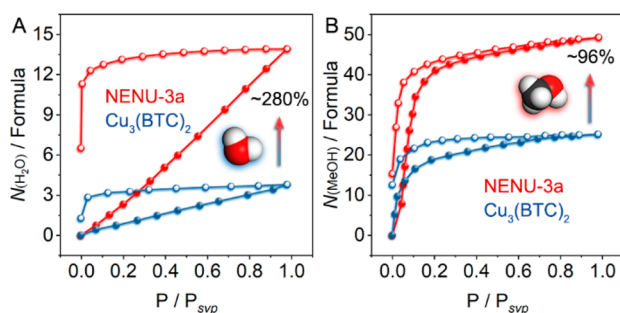


**Figure 2.** Vapor adsorption isotherms of NENU-3a (red) and Cu<sub>3</sub>(BTC)<sub>2</sub> (blue). (A) H<sub>2</sub>O; (B) MeOH.  $P_{\text{svp}}$  saturated vapor pressure. For comparison, the formula of Cu<sub>3</sub>(BTC)<sub>2</sub> is normalized as Cu<sub>12</sub>(BTC)<sub>8</sub>.

calculations also demonstrated the strong adsorption between water molecules/protons and Keggin HPW, thus affording high proton mobility around HPW.<sup>27</sup> Therefore, polar H<sup>+</sup>/H<sub>3</sub>O<sup>+</sup> and EdtaH<sub>2</sub><sup>2-</sup> (hydrated) will be preferentially adsorbed on the polar {100} crystal facets to etch NENU-3a rather than {111} facets covered by hydrophobic benzene rings, which is substantially consistent with a previous report that H<sup>+</sup> could not attach or enter the MOFs with a hydrophobic surface.<sup>23</sup> However, the many protons can attach/etch each position of NENU-3a with high concentrations, which thus weakened the aforementioned priority (Figure S4C vs Figure S4B). Therefore, it is particularly important to regulate the proton concentration for achieving both selectivity and effective etching simultaneously. It is well-known that EdtaH<sub>2</sub><sup>2-</sup> is a hexaprotic system that can accept or release H<sup>+</sup> (up to 6) at different pH values,<sup>26</sup> serving as source and reservoir for protons. In our etching experiments, a large amount of white precipitate appeared rapidly after the introduction of H<sub>3</sub>PO<sub>4</sub> into the clear EdtaH<sub>2</sub>Na<sub>2</sub> solution (Figure S13A,D), and correspondingly, the pH of the H<sub>3</sub>PO<sub>4</sub> solution increased from 2.22 to 3.16 (Figure S14A,B), which is attributed to the protonation of soluble EdtaH<sub>2</sub>Na<sub>2</sub> and the formation of Edta·xH<sup>+</sup> with low solubility. Furthermore, the main existing forms of Edta species are EdtaH<sub>4</sub> and EdtaH<sub>3</sub><sup>-</sup> at pH = 2.22 (Figure S15B), further indicating that EdtaH<sub>2</sub><sup>2-</sup> receives and stores H<sup>+</sup>. Therefore, H<sub>3</sub>PO<sub>4</sub> in collaboration with EdtaH<sub>2</sub>Na<sub>2</sub> provides

the initial etching with a low proton concentration. The dwindling H<sup>+</sup> can preferentially etch polar {100} facets and significantly weaken the etching of {110} facets (Figures S9 and S10), instead of many protons without EdtaH<sub>2</sub>Na<sub>2</sub> simultaneously etching the {100} and {110} crystal planes (Figure S4C). The initiation of selective etching by the on-demand storage of protons is illustrated in Scheme 1A and detailed Figure 3. In addition, another reason for not etching

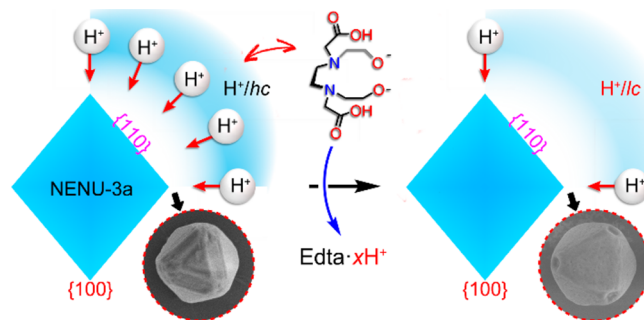


**Figure 3.** Schematic illustration of the selective etching initiated by on-demand proton storage. hc/lc: high/low concentration. The insets are the corresponding etched morphology.

the {110} crystal facet is the weakened chelating ability of EdtaH<sub>2</sub>Na<sub>2</sub> in H<sub>3</sub>PO<sub>4</sub>, which is attributed to the well-known “acid effect”. This corroborates the observation that the {110} crystal plane exposed with Cu<sup>II</sup> can be etched by EdtaH<sub>2</sub>Na<sub>2</sub> itself without H<sub>3</sub>PO<sub>4</sub> (Figure S12).

On the basis of the morphological evolution of NENU-3a/*x* and the intrinsic properties of EdtaH<sub>2</sub>Na<sub>2</sub> discussed above, we propose a chelation-assisted selective etching (CASE) mechanism. First, according to the previous discussion, the etching preferentially occurs on the {100} facet due to the initiation of dwindling H<sup>+</sup> (Figure 3) while BTC<sup>3-</sup> is protonated, accompanied by the breakage of the Cu-BTC coordination bonds (Scheme 1B). Subsequently, the liberated Cu<sup>2+</sup> is chelated by Edta·xH<sup>+</sup> in situ to form EdtaCu<sup>2+</sup> (Scheme 1C). Simultaneously, the H<sup>+</sup> stored by Edta·xH<sup>+</sup> is released (Scheme 1D), affording a local high proton concentration for further etching NENU-3a in situ (Scheme 1E). Therefore, EdtaH<sub>2</sub>Na<sub>2</sub> substantially realizes the enrichment of H<sup>+</sup>, which greatly deepens the selective etching, resulting in the rounded cubic NENU-3a with voids inside the {100} facets (Figure 1B). Moreover, the HPW released in situ also contributes to the selective etching (Scheme 1F). In addition, the capture of Cu<sup>2+</sup> by Edta·xH<sup>+</sup> effectively prevents any side reactions (impurity formation) (Scheme 1G) and also promotes the whole etching process, which can be concluded from the complete decomposition of NENU-3a caused by a further increase of added EdtaH<sub>2</sub>Na<sub>2</sub> (Figure S16). The deepening of the color of the final etching solution (Figure S17) and the increasing concentration of Cu<sup>II</sup>/HPW in the etching solution, i.e., the removed amount after etching of Cu<sup>II</sup>/HPW (Figure S18), further confirm the promotion of EdtaH<sub>2</sub>Na<sub>2</sub> on the etching.

Furthermore, when a high concentration of H<sub>3</sub>PO<sub>4</sub> with constant EdtaH<sub>2</sub>Na<sub>2</sub> is used, the overall etching is enhanced (particle size reduction, 1.1 μm) but the selectivity decreases (void shallowness) (Figure S19A,B), which is attributed to the stronger etching and weaker chelation caused by increased H<sup>+</sup> with a high initial concentration. More importantly, the

obtained NENU-3a/0.6 ( $\text{H}_3\text{PO}_4$ : 90 mM) is pure (Figure S19C,D), implying that  $\text{EdtaH}_2^{2-}$  can accept  $\text{H}^+$  and sequester  $\text{Cu}^{2+}$  so that NENU-3a does not completely collapse and the impurity phase does not form. Furthermore, when  $\text{EdtaH}_2\text{Na}_2$  was replaced with  $\text{EdtaH}_4$ , only cubic NENU-3a without voids was obtained (Figure S20). This is because the  $\text{H}^+$  enrichment effect of  $\text{EdtaH}_4$  is weaker than that of  $\text{EdtaH}_2\text{Na}_2$  (Figures S13F and S14B). The high initial concentration of protons leads to poor selectivity in NENU-3a etching, as discussed above. However, more  $\text{H}^+$  released after the chelation between  $\text{EdtaH}_4$  and  $\text{Cu}^{2+}$  further strengthens the external etching (Figure S14C), along with the transformation of octahedral NENU-3a to small cubic counterparts (Figure S20). When the  $\text{H}_3\text{PO}_4$  concentration is carefully controlled so that the total  $\text{H}^+$  content of  $\text{H}_3\text{PO}_4$  and  $\text{EdtaH}_4$  was identical with that of 60 mM  $\text{H}_3\text{PO}_4$  containing  $\text{EdtaH}_2\text{Na}_2$  ( $x = 0.6$ ), the clear voids are created inside etched NENU-3a (Figure S21). This suggests that the low initial proton concentration and sustained release effect of  $\text{EdtaH}_4$  on  $\text{H}^+$ , i.e., the enrichment effect of  $\text{EdtaH}_2\text{Na}_2$  on  $\text{H}^+$ , are crucial for selective etching of the  $\{100\}$  crystal plane on NENU-3a. The above results further demonstrate the proposed CASE mechanism. In addition, the etching without  $\text{EdtaH}_2\text{Na}_2$  being involved (Figure S4C) can also be rationalized by the CASE mechanism. The more  $\text{H}^+$  provided by  $\text{H}_3\text{PO}_4$  directly etches NENU-3a ( $\{100\}$  and  $\{110\}$  facets) and is subsequently consumed by  $\text{BTC}^{3-}$ . Therefore, the etching is quickly terminated, and deeper etching could not be performed (Figure S22). In order to further elucidate the selective etching, the nonoctahedral particles also were etched. As expected, the etching still occurs preferentially on the  $\{100\}$  crystal plane on cuboctahedral NENU-3a, which further demonstrates the selectivity of the  $\{100\}$  crystal facet (Figure S23). According to the previous discussion, the selective etching of the  $\{100\}$  crystal plane originates from the exposure of the polar HPW. Therefore, the etching of  $\text{Cu}_3(\text{BTC})_2$  without HPW is meaningful to explain the aforementioned selectivity. However,  $\text{Cu}_3(\text{BTC})_2$  rapidly and completely decomposed due to poor stability (Figure S24), which strengthens that the introduction of HPW improves the framework stability, consistent with our previous reports.<sup>6,14</sup>

**Surface Energies of Crystal Facets in NENU-3a.** Besides experiments and structural analysis, the effect of crystal surface energy on selective etching was further considered. Figure S1B–D shows the surface structures of different crystal planes in NENU-3a. As shown in Figure S25, the slicing plane of  $\{111\}$ ,  $\{110\}$ , and  $\{100\}$  in NENU-3a is created, which is based on two factors jointly leading to the minimal energy required to create surfaces. (i) The stabilizing effect from HPW on the framework,<sup>6,10</sup> i.e., the slicing plane cutting through HPW with its destroyed integrity, should be preferably avoided. (ii) While the Cu–O bonds (O from acetate groups of BTC) are relatively much weaker than the C–C and C–O covalent bonds of BTC ligands, only the minimum Cu–O bonds per surface area are broken when surface is created.<sup>28</sup> Accordingly, the surface energy  $\gamma$  is then defined as follows:

$$\gamma_{hkl} = \frac{N_{\text{Cu-O}} \times E_{\text{Cu-O}}}{S}$$

where  $N_{\text{Cu-O}}$  is the number of Cu–O bonds to be broken,  $E_{\text{Cu-O}}$  is the bond energy of Cu–O bond, and  $S$  is the surface area for the analysis. According to the single crystal structure of NENU-3a, there is only one Cu–O bond in the asymmetric

unit (Figure S26), which is conducive to the analysis of surface energy. In order to facilitate the calculation of the number of Cu–O bonds to be broken per surface area, the unit cell transformation of NENU-3a was performed by VESTA 3.<sup>29</sup> The transformed unit cell and unit cell parameters are shown in Figure 4 and Table S1, and the corresponding slicing planes

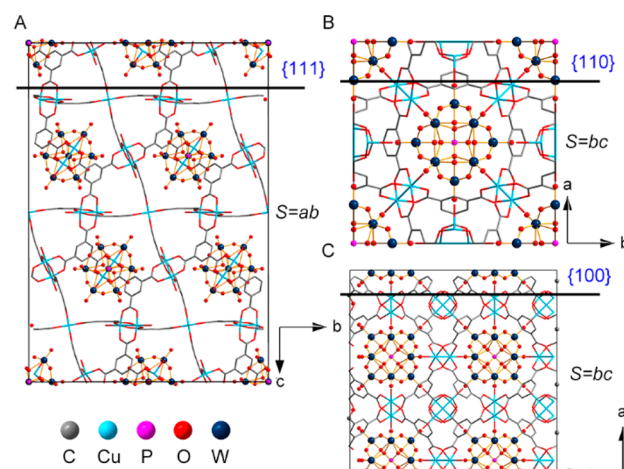


**Figure 4.** Transformed unit cell for analysis and the slicing planes indicated by lines for facets. (A)  $\{111\}$ , (B)  $\{110\}$ , and (C)  $\{100\}$ . All H atoms are omitted for clarity.

are shown in Figure 4 by a line and Figures S27–S29. According to the above equation, the calculated surface energies of the crystal planes are as follows:  $\gamma_{111}$  ( $2.011E_{\text{Cu-O}}$ ) <  $\gamma_{110}$  ( $3.268E_{\text{Cu-O}}$ ) <  $\gamma_{100}$  ( $4.621E_{\text{Cu-O}}$ ) (see Figures S27–S29 for details). Further, the bond energy of the Cu–O bond is 287.4 kJ/mol,<sup>30</sup> so the corresponding surface energies are  $0.960 \text{ J m}^{-2}$  ( $\{111\}$ ),  $1.560 \text{ J m}^{-2}$  ( $\{110\}$ ), and  $2.205 \text{ J m}^{-2}$  ( $\{100\}$ ). The surface energy results further support our proposed selectivity of etching. The exposure of more metal clusters on the  $\{100\}$  facet contributes to the higher energy, which is contrary to the  $\{111\}$  facet. The metal clusters on the  $\{100\}$  plane are arranged so that the exposed window of HPW faces outward (Figure S1B), while the hydrophobic benzene ring faces outward on the  $\{111\}$  facet (Figure S1D). It is generally known that hydrophilicity is proportional to surface energy. Therefore, polar protons with low concentration tend to etch the  $\{100\}$  facet. When the proton concentration increases, the  $\{110\}$  crystal plane with a slightly lower surface energy is also etched, as shown in the experimental results (Figure S4B,C). In addition, the higher energy of the  $\{100\}$  facet is also consistent with the better catalytic activity reported before.<sup>11</sup>

**Hierarchically Porous Structure Created by Etching.** To further explore the hierarchical structure of etched NENU-3a,  $\text{N}_2$  adsorption/desorption measures were performed. The few mesopores in NENU-3a are due to the spatial effect of chloroform enrichment areas, consistent with our previous reports.<sup>17</sup> In sharp contrast, the etched NENU-3a possesses obvious mesopores, which are characterized by the typical type IV isotherms in Figure 5A.<sup>31</sup> Nevertheless, the low  $\text{N}_2$  adsorption capacity and small mesopore volume of NENU-3a/0.0 are ascribed to the impurity phase. The specific surface area and mesopore volume of NENU-3a/0.6 are  $654.84 \text{ m}^2/\text{g}$  and  $0.2032 \text{ cm}^3/\text{g}$ , which are higher than that of NENU-3a/0.4 ( $564.58 \text{ m}^2/\text{g}$  and  $0.1494 \text{ cm}^3/\text{g}$ ) (Table S2). The increase of

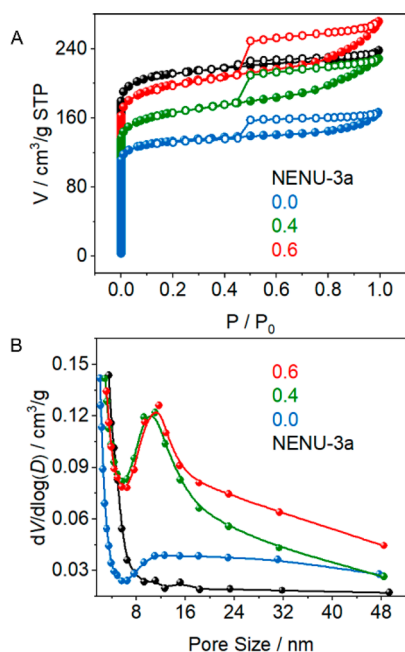


**Figure 5.** (A)  $\text{N}_2$  adsorption/desorption isotherms and (B) pore diameter distribution of NENU-3a and NENU-3a/ $x$ .

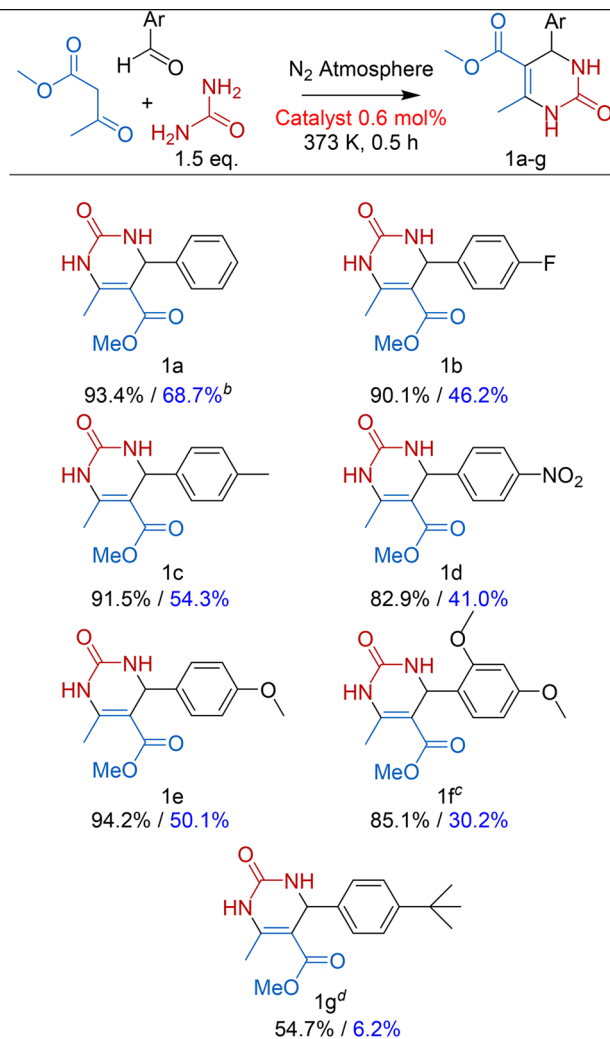
the specific surface area and mesopore volume of NENU-3a/0.6 arises from the reduced particle size (around  $1.4 \mu\text{m}$ ) and promoted etching triggered by more  $\text{EdtaH}_2\text{Na}_2$ , which is in accord with the SEM results described earlier (Figure 1B). The significant  $\text{N}_2$  uptake within the low-pressure region indicates that the intrinsic micropores of the NENU-3a are well maintained;<sup>32</sup> namely, the parent crystalline framework is not completely destroyed after etching, which agrees well with the XRD results (Figure S8). Despite the distribution of mesopores within 2–50 nm (Figure 5B), the mesopore diameter of NENU-3a/0.6 is mainly centered at around 12 nm. Such large-sized mesopores play an important role in promoting mass transfer and diffusion of bulky guest species.<sup>21</sup> According to the CASE mechanism, the mesopores originate from the etching in NENU-3a interior by the protons penetrating through the  $\{100\}$  crystal facets, resulting in partial disassociation of the NENU-3a framework. For the incompletely etched NENU-3a/0.6, the sponge-like structure in the  $\{100\}$  crystal plane indirectly indicates that the etching occurs internally (Figure S10C). In addition, the higher transparency of the corresponding TEM images (Figure S10C1,E1) compared with that of NENU-3a (Figure S30) also demonstrate the existence of mesoporous structures.<sup>22</sup> Of note, the stability of etched NENU-3a is not undermined by the introduction of mesopores and voids, as evidenced by the thermogravimetric analysis (Figure S31).

Besides  $\text{EdtaH}_2\text{Na}_2$ , the etching process is also related to time. In the first 2 h, the selective etching of the  $\{100\}$  facet was significantly more severe than that of the  $\{110\}$  crystal facet (Figure S32A), which corroborates well with the previous discussion that reduced  $\text{H}^+$  with  $\text{Edta} \cdot x\text{H}^+$  preferentially etches the facets exposed by HPW (i.e.,  $\{100\}$ ). With the further extension of the etching time (6 h), some fractured particles appeared, which may be due to the further etching of  $\text{H}^+$  and prolonged stirring and collision (Figure S32B). As expected, all the NENU-3a/0.6 with different etching times hold meso-

pores, as evidenced by the  $\text{N}_2$  adsorption/desorption isotherms and pore size distribution analysis (Figure S33).

**Enhanced Catalytic Performance for Biginelli Reactions.** The diversely functionalized 3,4-dihydropyrimidin-2(1H)-ones (DHPMs), synthesized from urea,  $\beta$ -ketoesters, and aryl aldehydes by acid-catalyzed Biginelli reactions (Table 1), represent a broad range of promising pharmacological

**Table 1.** Biginelli Reactions Catalyzed by NENU-3a and NENU-3a/0.6<sup>a</sup>



<sup>a</sup>Isolated yields are shown. <sup>b</sup>The yields in blue belong to the reaction catalyzed by NENU-3a. <sup>c</sup>1 h. <sup>d</sup>5 h.

activities.<sup>33</sup> Despite the fact that some MOF catalysts have exhibited excellent activity for the Biginelli reactions, the microporous mass-transportation limitations still exist when the bulky reactants and products are involved.<sup>34,35</sup> Considering the macro-mesoporous mass transfer channels and exposed HPW sites, we intend to explore the catalytic activity of NENU-3a/0.6 for the Biginelli reactions. In comparison with NENU-3a, NENU-3a/0.6 exhibited faster reaction kinetics (Figure S34A) and more outstanding catalytic performance in the reaction involving benzaldehyde (Table 1, 1a). Further, when benzaldehyde was extended to other substituted ones (Table S3), NENU-3a/0.6 always exhibited more excellent catalytic performance, especially for bulky substituents (Figure

S34B and Table 1), which is due to the enhanced mass transferring efficiency and readily accessible active sites on the hierarchical structure. In addition, compared to NENU-3a, NENU-3a/0.0 with only mesopores also exhibited improved catalytic activity (Figure S34), which further strengthens the diffusion convenience brought by mesoporous channels. However, the poorer catalytic behavior of NENU-3a/0.0 than that of NENU-3a/0.6 is attributed to the impurity phase and the limitedly exposed catalytic sites (Figure S34). All of the DHPM products were confirmed by  $^1\text{H}$  nuclear magnetic resonance (Figures S35–S41), and the recovered catalyst was used in the subsequent cycle experiments. After several catalytic runs, the yield can still be maintained at 90%, indicating that the catalytic performance of the NENU-3a/0.6 is not obviously attenuated during the catalysis (Figure S42). Moreover, the well-maintained morphology, crystallinity, and pore structure reflected by the SEM image, XRD pattern, and  $\text{N}_2$  adsorption studies of the recovered NENU-3a/0.6 further confirmed the good stability and recyclability of the catalyst (Figure S43).

## CONCLUSIONS

In summary, we developed a chelation-assisted etching strategy to construct hierarchical POM@MOF. The chelation not only successfully captures the liberated metal ions to avoid impurity phases but also significantly promotes the forward movement of the etching equilibrium to facilitate the etching process. More importantly, the on-demand storage and secondary release of protons achieved by the chelator result in a high–low–high switch in the  $\text{H}^+$  concentration. The switch effectively initiates and promotes the selective etching, resulting in the precise definition of the etched macrovoids in the POM@MOF with desired morphology. Moreover, the definite mesopores can also be created during etching, which greatly enhances the diffusion efficiency of the reaction species. Since the anisotropy of crystals and chelation between chelators and metal ions are universal, this chelation-assisted etching strategy is expected to be applied to the synthesis of other hierarchical MOFs. More interestingly, because of the distinct structure of various MOFs, the etching may cause additional unexpected and meaningful findings, to be explored in the future.

## EXPERIMENTAL SECTION

**Procedure for the Etching Experiment.** As-prepared mono-dispersed NENU-3a (details in the Supporting Information Section S3, 50 mg) was activated under vacuum at  $120\text{ }^\circ\text{C}$  and then soaked in 5 mL of a mixed solution of MeOH and  $\text{H}_2\text{O}$  (V/V, 1/1) with different concentrations of phosphoric acid ( $\text{H}_3\text{PO}_4$ ) and different amounts of ethylenediaminetetraacetic acid disodium salt dihydrate ( $\text{EdtaH}_2\text{Na}_2\cdot 2\text{H}_2\text{O}$ , abbreviated as  $\text{EdtaH}_2\text{Na}_2$ ). All solutions with NENU-3a were sonicated for 3 min at room temperature and then kept at  $50\text{ }^\circ\text{C}$  for 4 h in a heater. For time-controlled etching experiments, the etching time was varied from 2 to 6 h in 60 mM  $\text{H}_3\text{PO}_4$ . The final products were washed with  $\text{H}_2\text{O}$  and EtOH two times each and dried under  $50\text{ }^\circ\text{C}$ .

**Procedure for the Catalytic Synthesis of 3,4-Dihydropyrimidin-2(1H)-ones.** The mixture of aromatic aldehyde (1.0 mmol), ethyl acetoacetate (1.0 mmol), urea (1.5 mmol), and activated catalyst (0.6 mol %) was reacted at  $100\text{ }^\circ\text{C}$  under a nitrogen atmosphere. The progress of the reaction was monitored by thin layer chromatography (TLC). Then, the cooling reaction mixture was dispersed in 20 mL of ethyl acetate and filtered to recover the catalyst. The recovered catalyst was washed with *N,N*-dimethylformamide, water, and anhydrous ethanol two times prior to its reuse in the next cycles.

The ethyl acetate was evaporated, and the crude product was further purified by recrystallization from *n*-hexane/ethyl acetate (3:1) to afford pure 3,4-dihydropyrimidin-2(1H)-ones. All products were characterized by  $^1\text{H}$  NMR.

## ASSOCIATED CONTENT

### Supporting Information

The Supporting Information is available free of charge at <https://pubs.acs.org/doi/10.1021/acs.chemmater.0c00440>.

cell\_trans\_NENU-3a\_111 (CIF)

cell\_trans\_NENU-3a\_110 (CIF)

cell\_trans\_NENU-3a\_100 (CIF)

Additional experimental details, materials, characterizations, crystal structure of NENU-3a, SEM images, element mapping, XRD patterns, FTIR patterns, structure diagrams, TEM images, EDX elemental line scans, photographs of reactions and experiments, pH of solutions, fractional composition diagrams, UV-vis spectroscopy, the etching process, generated slicing planes, unit cell parameters, views of the surfaces, porosity properties, TGA curves,  $\text{N}_2$  adsorption/desorption isotherms and pore diameter distribution, conversion versus reaction time, molecular size of aromatic aldehyde substrates for Biginelli Reactions, and  $^1\text{H}$  NMR spectra (PDF)

## AUTHOR INFORMATION

### Corresponding Author

Shuxia Liu – Key Laboratory of Polyoxometalate Science of the Ministry of Education, School of Chemistry, Northeast Normal University, Changchun, Jilin 130024, P. R. China;  
[orcid.org/0000-0003-0235-8594](https://orcid.org/0000-0003-0235-8594); Email: [liusx@nenu.edu.cn](mailto:liusx@nenu.edu.cn)

### Authors

Zhong Zhang – Key Laboratory of Polyoxometalate Science of the Ministry of Education, School of Chemistry, Northeast Normal University, Changchun, Jilin 130024, P. R. China

Yunwen Tao – Department of Chemistry, Southern Methodist University, Dallas, Texas 75275-0314, United States

Hongrui Tian – Key Laboratory of Polyoxometalate Science of the Ministry of Education, School of Chemistry, Northeast Normal University, Changchun, Jilin 130024, P. R. China

Qian Yue – Key Laboratory of Polyoxometalate Science of the Ministry of Education, School of Chemistry, Northeast Normal University, Changchun, Jilin 130024, P. R. China

Shumei Liu – Key Laboratory of Polyoxometalate Science of the Ministry of Education, School of Chemistry, Northeast Normal University, Changchun, Jilin 130024, P. R. China

Yiwei Liu – Key Laboratory of Polyoxometalate Science of the Ministry of Education, School of Chemistry, Northeast Normal University, Changchun, Jilin 130024, P. R. China

Xiaohui Li – Key Laboratory of Polyoxometalate Science of the Ministry of Education, School of Chemistry, Northeast Normal University, Changchun, Jilin 130024, P. R. China

Ying Lu – Key Laboratory of Polyoxometalate Science of the Ministry of Education, School of Chemistry, Northeast Normal University, Changchun, Jilin 130024, P. R. China;

[orcid.org/0000-0002-8828-169X](https://orcid.org/0000-0002-8828-169X)

Zhixia Sun – Key Laboratory of Polyoxometalate Science of the Ministry of Education, School of Chemistry, Northeast Normal University, Changchun, Jilin 130024, P. R. China

Elfi Kraka – Department of Chemistry, Southern Methodist University, Dallas, Texas 75275-0314, United States;  
orcid.org/0000-0002-9658-5626

Complete contact information is available at:  
<https://pubs.acs.org/10.1021/acs.chemmater.0c00440>

## Notes

The authors declare no competing financial interest.

## ACKNOWLEDGMENTS

This work was financially supported by the National Natural Science Foundation of China (grants 21872021, 21671033, and 21901135). Y.T. and E.K. thank SMU for providing generous computational resources.

## REFERENCES

- (1) Furukawa, H.; Cordova, K. E.; O’Keeffe, M.; Yaghi, O. M. The Chemistry and Applications of Metal–Organic Frameworks. *Science* **2013**, *341*, 1230444–1230455.
- (2) Yang, D.; Gates, B. C. Catalysis by Metal Organic Frameworks: Perspective and Suggestions for Future Research. *ACS Catal.* **2019**, *9*, 1779–1798.
- (3) Li, D.; Xu, H.-Q.; Jiao, L.; Jiang, H.-L. Metal–Organic Frameworks for Catalysis: State of the Art, Challenges, and Opportunities. *EnergyChem.* **2019**, *1*, 100005–100043.
- (4) Chen, L.; Xu, Q. Metal–Organic Framework Composites for Catalysis. *Matter* **2019**, *1*, 57–89.
- (5) Huang, Y.-B.; Liang, J.; Wang, X.-S.; Cao, R. Multifunctional Metal–Organic Framework Catalysts: Synergistic Catalysis and Tandem Reactions. *Chem. Soc. Rev.* **2017**, *46*, 126–157.
- (6) Sun, C.-Y.; Liu, S.-X.; Liang, D.-D.; Shao, K.-Z.; Ren, Y.-H.; Su, Z.-M. Highly Stable Crystalline Catalysts Based on a Microporous Metal–Organic Framework and Polyoxometalates. *J. Am. Chem. Soc.* **2009**, *131*, 1883–1888.
- (7) Ma, F. J.; Liu, S. X.; Sun, C. Y.; Liang, D. D.; Ren, G. J.; Wei, F.; Chen, Y. G.; Su, Z. M. A Sodalite-Type Porous Metal–Organic Framework with Polyoxometalate Templates: Adsorption and Decomposition of Dimethyl Methylphosphonate. *J. Am. Chem. Soc.* **2011**, *133*, 4178–4181.
- (8) Du, D.-Y.; Qin, J.-S.; Li, S.-L.; Su, Z.-M.; Lan, Y.-Q. Recent Advances in Porous Polyoxometalate-Based Metal–Organic Framework Materials. *Chem. Soc. Rev.* **2014**, *43*, 4615–4632.
- (9) Li, X.; Liu, Y.; Liu, S.; Wang, S.; Xu, L.; Zhang, Z.; Luo, F.; Lu, Y.; Liu, S. A Gel-Like/Freeze-Drying Strategy to Construct Hierarchically Porous Polyoxometalate-Based Metal–Organic Framework Catalysts. *J. Mater. Chem. A* **2018**, *6*, 4678–4685.
- (10) Bajpe, S. R.; Kirschhock, C. E. A.; Aerts, A.; Breynaert, E.; Absillis, G.; Parac-Vogt, T. N.; Giebler, L.; Martens, J. A. Direct Observation of Molecular-Level Template Action Leading to Self-Assembly of a Porous Framework. *Chem. - Eur. J.* **2010**, *16*, 3926–3932.
- (11) Liu, Y.; Liu, S.; He, D.; Li, N.; Ji, Y.; Zheng, Z.; Luo, F.; Liu, S.; Shi, Z.; Hu, C. Crystal Facets Make a Profound Difference in Polyoxometalate-Containing Metal–Organic Frameworks as Catalysts for Biodiesel Production. *J. Am. Chem. Soc.* **2015**, *137*, 12697–12703.
- (12) Xu, X.; Lu, Y.; Yang, Y.; Nosheen, F.; Wang, X. Tuning the Growth of Metal–Organic Framework Nanocrystals by Using Polyoxometalates as Coordination Modulators. *Science China Materials* **2015**, *58*, 370–377.
- (13) Liu, S.-M.; Zhang, Z.; Li, X.; Jia, H.; Ren, M.; Liu, S. Ti-Substituted Keggin-Type Polyoxotungstate as Proton and Electron Reservoir Encaged into Metal–Organic Framework for Carbon Dioxide Photoreduction. *Adv. Mater. Interfaces* **2018**, *5*, 1801062–1801068.
- (14) Liu, Y.; Yang, X.; Miao, J.; Tang, Q.; Liu, S.; Shi, Z.; Liu, S. Polyoxometalate-Functionalized Metal–Organic Frameworks with Improved Water Retention and Uniform Proton-Conducting Path-

ways in Three Orthogonal Directions. *Chem. Commun.* **2014**, *50*, 10023–10026.

(15) Tian, H.-R.; Liu, Y.-W.; Zhang, Z.; Liu, S.-M.; Dang, T.-Y.; Li, X.-H.; Sun, X.-W.; Lu, Y.; Liu, S.-X. A Multicentre Synergistic Polyoxometalate-Based Metal–Organic Framework for One-Step Selective Oxidative Cleavage of  $\beta$ -O-4 Lignin Model Compounds. *Green Chem.* **2020**, *22*, 248–255.

(16) Zhong, X.; Lu, Y.; Luo, F.; Liu, Y.; Li, X.; Liu, S. A Nanocrystalline POM@MOFs Catalyst for the Degradation of Phenol: Effective Cooperative Catalysis by Metal Nodes and Pom Guests. *Chem. - Eur. J.* **2018**, *24*, 3045–3051.

(17) Zhang, Z.; Liu, Y.-W.; Tian, H.-R.; Li, X.-H.; Liu, S.-M.; Lu, Y.; Sun, Z.-X.; Liu, T.; Liu, S.-X. Polyoxometalate-Based Metal–Organic Framework Fractal Crystals. *Matter* **2020**, *2*, 250–260.

(18) Zhang, Q.; Mayoral, A.; Terasaki, O.; Zhang, Q.; Ma, B.; Zhao, C.; Yang, G.; Yu, J. Amino Acid-Assisted Construction of Single-Crystalline Hierarchical Nanozeolites Via Oriented-Aggregation and Intraparticle Ripening. *J. Am. Chem. Soc.* **2019**, *141*, 3772–3776.

(19) Teng, J.; Chen, M.; Xie, Y.; Wang, D.; Jiang, J.-J.; Li, G.; Wang, H.-P.; Fan, Y.; Wei, Z.-W.; Su, C.-Y. Hierarchically Porous Single Nanocrystals of Bimetallic Metal–Organic Framework for Nano-reactors with Enhanced Conversion. *Chem. Mater.* **2018**, *30*, 6458–6468.

(20) Shen, K.; Zhang, L.; Chen, X.; Liu, L.; Zhang, D.; Han, Y.; Chen, J.; Long, J.; Luque, R.; Li, Y.; Chen, B. Ordered Macroporous Metal–Organic Framework Single Crystals. *Science* **2018**, *359*, 206–210.

(21) Kirchon, A.; Li, J.; Xia, F.; Day, G. S.; Becker, B.; Chen, W.; Sue, H.-J.; Fang, Y.; Zhou, H.-C. Modulation Versus Templating: Fine-Tuning of Hierarchically Porous PCN-250 Using Fatty Acids to Engineer Guest Adsorption. *Angew. Chem., Int. Ed.* **2019**, *58*, 12425–12430.

(22) Koo, J.; Hwang, I.-C.; Yu, X.; Saha, S.; Kim, Y.; Kim, K. Hollowing out Mofs: Hierarchical Micro- and Mesoporous MOFs with Tailorable Porosity Via Selective Acid Etching. *Chem. Sci.* **2017**, *8*, 6799–6803.

(23) Hu, M.; Ju, Y.; Liang, K.; Suma, T.; Cui, J.; Caruso, F. Void Engineering in Metal–Organic Frameworks Via Synergistic Etching and Surface Functionalization. *Adv. Funct. Mater.* **2016**, *26*, 5827–5834.

(24) Avci, C.; Ariñez-Soriano, J.; Carné-Sánchez, A.; Guillerm, V.; Carbonell, C.; Imaz, I.; Maspoch, D. Post-Synthetic Anisotropic Wet-Chemical Etching of Colloidal Sodalite ZIF Crystals. *Angew. Chem., Int. Ed.* **2015**, *54*, 14417–14421.

(25) Liu, W.; Huang, J.; Yang, Q.; Wang, S.; Sun, X.; Zhang, W.; Liu, J.; Huo, F. Multi-Shelled Hollow Metal–Organic Frameworks. *Angew. Chem., Int. Ed.* **2017**, *56*, 5512–5516.

(26) Harris, D. C. *Quantitative Chemical Analysis*, 8th ed.; Macmillan: 2010.

(27) Janik, M. J.; Davis, R. J.; Neurock, M. Anhydrous and Water-Assisted Proton Mobility in Phosphotungstic Acid. *J. Am. Chem. Soc.* **2005**, *127*, 5238–5245.

(28) Amirjalayer, S.; Tafipolsky, M.; Schmid, R. Surface Termination of the Metal–Organic Framework HKUST-1: A Theoretical Investigation. *J. Phys. Chem. Lett.* **2014**, *5*, 3206–3210.

(29) Momma, K.; Izumi, F. Vesta 3 for Three-Dimensional Visualization of Crystal, Volumetric and Morphology Data. *J. Appl. Crystallogr.* **2011**, *44*, 1272–1276.

(30) Luo, Y.-R. *Comprehensive Handbook of Chemical Bond Energies*; CRC Press: 2007; DOI: 10.1201/9781420007282.

(31) Thommes, M.; Kaneko, K.; Neimark Alexander, V.; Olivier James, P.; Rodriguez-Reinoso, F.; Rouquerol, J.; Sing Kenneth, S. W. Physisorption of Gases, with Special Reference to the Evaluation of Surface Area and Pore Size Distribution (IUPAC Technical Report). *Pure Appl. Chem.* **2015**, *87*, 1051.

(32) Qiu, L.-G.; Xu, T.; Li, Z.-Q.; Wang, W.; Wu, Y.; Jiang, X.; Tian, X.-Y.; Zhang, L.-D. Hierarchically Micro- and Mesoporous Metal–Organic Frameworks with Tunable Porosity. *Angew. Chem., Int. Ed.* **2008**, *47*, 9487–9491.

(33) Kappe, C. O. Recent Advances in the Biginelli Dihydropyrimidine Synthesis. New Tricks from an Old Dog. *Acc. Chem. Res.* **2000**, *33*, 879–888.

(34) Verma, A.; De, D.; Tomar, K.; Bharadwaj, P. K. An Amine Functionalized Metal–Organic Framework as an Effective Catalyst for Conversion of CO<sub>2</sub> and Biginelli Reactions. *Inorg. Chem.* **2017**, *56*, 9765–9771.

(35) Pal, T. K.; De, D.; Senthilkumar, S.; Neogi, S.; Bharadwaj, P. K. A Partially Fluorinated, Water-Stable Cu(II)–MOF Derived Via Transmetalation: Significant Gas Adsorption with High CO<sub>2</sub> Selectivity and Catalysis of Biginelli Reactions. *Inorg. Chem.* **2016**, *55*, 7835–7842.